AIAA JOURNAL
Vol. 46, No. 2, February 2008

Computational Study of Unsteady Low-Reynolds-Number Airfoil Aerodynamics Using Moving Overlapping Meshes

Dominic D. J. Chandar* and M. Damodaran†
Nanyang Technological University, Singapore 639798, Republic of Singapore

DOI: 10.2514/1.31499

One of the challenging areas of research motivated by insects and birds is to predict instantaneous unsteady forces on a rapidly maneuvering object. The basic underlying mechanisms of force production are well known and have been established by early researchers through extensive experiments and numerical computations supported by classical theories of unsteady aerodynamics. Nevertheless, to date, experiments and numerical computations of this problem have been focused either on fluid mechanics alone or on fluid mechanics coupled with structural mechanics. The rigid-body dynamics of plunging/pitching/flapping bodies has received less attention. In view of this, an attempt is made here to simulate the rigid-body dynamics of plunging airfoils in incompressible low-Reynolds-number flow in the range of $10 < Re < 4.5 \times 10^4$ by solving the incompressible Navier–Stokes equations on moving overlapping meshes. The need for a sharp trailing edge is demonstrated by comparing the computed thrust and forward speed for airfoils with different trailing-edge topologies when plunged in zero freestream velocity. The effect of freestream and ground proximity was also analyzed for active flight.

Nomenclature

C_{Di}	=	divergence damping coefficient
C_f	=	skin friction coefficient
$C_{L_{\max}}$	=	maximum lift coefficient
C_p	=	pressure coefficient
C_T	=	thrust coefficient ($-C_D$, drag coefficient)
c	=	chord length or mean aerodynamic chord
e_i	=	principle axes ($i = 1, 2, 3$)
$\boldsymbol{F}$	=	body force
$\boldsymbol{F}_A$	=	aerodynamic forces (lift and drag)
f	=	plunge frequency
$\boldsymbol{h}$	=	angular momentum
h_0	=	plunge amplitude scaled by chord
I	=	moment of inertia
k	=	reduced frequency, $\omega c/U_\infty = 2\pi f c/U_\infty$
M	=	mass
p	=	pressure
Re	=	Reynolds number, $U_\infty c/\upsilon$
St	=	Strouhal number, kh_0
$\boldsymbol{T}$	=	aerodynamic moment/torque
U_∞	=	freestream velocity
$\boldsymbol{u}$	=	velocity field (u, v, w)
V_p	=	peak plunge velocity
υ	=	kinematic viscosity
$\boldsymbol{x}_{\mathrm{cm}}$	=	center of mass
λ	=	wake wavelength
ρ	=	fluid density
ω	=	angular velocity

Presented as Paper 4559 at the AIAA 25th Applied Aerodynamics Conference, Miami, FL, 25–28 June 2007; received 9 April 2007; revision received 11 July 2007; accepted for publication 18 September 2007. Copyright © 2007 by the American Institute of Aeronautics and Astronautics, Inc. All rights reserved. Copies of this paper may be made for personal or internal use, on condition that the copier pay the $10.00 per-copy fee to the Copyright Clearance Center, Inc., 222 Rosewood Drive, Danvers, MA 01923; include the code 0001-1452/08 $10.00 in correspondence with the CCC.

*Graduate Student, Division of Thermal and Fluids Engineering, School of Mechanical and Aerospace Engineering, 50 Nanyang Avenue; domi0002@ntu.edu.sg. Student Member AIAA.

†Associate Professor, Division of Thermal and Fluids Engineering, School of Mechanical and Aerospace Engineering, 50 Nanyang Avenue; mdamodaran@ntu.edu.sg. Associate Fellow AIAA.

I. Introduction

THERE has been a sudden surge in the study of bird and insect flight during the past few years, primarily motivated by the need for developing control-efficient micro aerial vehicles based on theories of unsteady aerodynamics. Birds and insects have baffled humans for thousands of years with their extraordinary flying capability coupled with agile movements. Understanding the behavior of flying creatures requires an integration of different disciplines such as biology, aerodynamics, and control. Biologists in association with fluid dynamists have been trying to understand the mechanics of propulsion by means of experimentation on model birds and flapping wings. An extensive review can be found in Sun and Tang [1], Ramamurti et al. [2], Ellington [3], Shyy et al. [4], Liu and Kawachi [5], and Wang et al. [6]. The advent of computational fluid dynamics has further enhanced the interest in understanding unsteady aerodynamics by enabling researchers to experiment with a variety of two- and three-dimensional aerodynamic configurations on efficient computers with minimal turnaround time. Liu et al. [5,7] modeled a hovering insect wing using the pseudocompressibility method and obtained qualitative features of the three-dimensional unsteady flowfield. Tuncer and Platzer [8] investigated turbulent flow computations for plunging and pitching oscillations of airfoils at various reduced frequencies and verified their results with water-tunnel experiments. Numerical simulations based on panel methods by Jones et al. [9], vorticity-stream function formulation by Sengupta et al. [10], and Navier–Stokes solutions on overlapping meshes by Tuncer and Platzer [11] have been used to obtain qualitative flow features and aerodynamic forces and moments of a flapping wing. Yet, the application of computational fluid dynamics to predict highly accurate results for moving bodies is limited to simple geometries or simple movements and there has not been much research in simulating passive-form flapping (i.e., coupled Navier–Stokes and rigid-body dynamics) and analyzing the aerodynamic effects of small topological changes in the configurations. Pesavento and Wang [12] computationally demonstrated the passive flight of a falling object under gravity and determined various bounds on its flutter and tumble. Lai and Platzer [13] experimentally investigated the effect of a sharp trailing edge based on the observation of Bennet et al. [14], but their analysis was limited to only a single case in active flight. Also, flapping flight in the proximity of the ground has been studied experimentally and numerically by Jones et al. [15], and this form of flight demonstrated substantial improvement in thrust and propulsive efficiencies. Yet, this was limited to a single NACA 0014 airfoil. Hence, the objective of the present study is to explore the effects of trailing-edge geometry and ground proximity on thrust

production for both active and passive flight at very low Reynolds numbers by solving the Navier–Stokes equations coupled with rigid-body dynamics on moving overlapping meshes. Moving overlapping meshes is an efficient approach for the present problem, because the meshes need not be regenerated as the solution evolves, as opposed to conventional techniques in which the meshes are either regenerated or deformed after a time step. The object-oriented code OverBlown [16], which is based on the Overture [17] framework, is used for solving the incompressible Navier–Stokes equations on moving overlapping meshes. In the following sections, the numerical method followed by extensive validation studies and results and discussions on various numerical experiments is presented.

II. Governing Equations and Numerical Method

The complete description of the numerical method, implementation of the boundary conditions, interpolation on the overlapping mesh, and convergence studies can be found in Henshaw [16]. However, for the sake of completeness, an outline of the numerical method is provided here. The governing equations are the time-dependent incompressible Navier–Stokes equations:

$$\mathbf{u}_t + (\mathbf{u}\cdot\nabla)\mathbf{u} + \frac{\nabla p}{\rho} = \upsilon\Delta\mathbf{u} + \mathrm{F}, \qquad \nabla\cdot\mathbf{u} = 0 \tag{1}$$

These equations are discretized in space on a system of overlapping meshes (Fig. 1). Each of those meshes is a mapping from the physical domain with coordinates $\boldsymbol{x}$ to the computational domain with coordinates $\boldsymbol{r}$. This mapping is defined in Henshaw [16] and Brown et al. [17] as $\boldsymbol{x} = \boldsymbol{G}(\boldsymbol{r})$. For a mesh that is moving with the body (rigidly), this mapping is a function of time given by $\boldsymbol{x} = \boldsymbol{G}(\boldsymbol{r}, t)$ $(t = \tau)$. Hence, the Navier–Stokes equations (1) in the reference frame moving with the mesh is transformed to

$$\begin{gathered}\mathbf{u}_\tau + [(\mathbf{u}_i - \dot{G}_i)(\partial_{x_i} r_j)\partial_{r_j}]\mathbf{u} + (\partial_{x_i} r_j)\partial_{r_j}\frac{p}{\rho} = \upsilon\tilde{\Delta}\mathbf{u} + \mathbf{F} \\ \tilde{\Delta}p + \rho\Sigma_i\tilde{\nabla}\mathbf{u}_i\cdot\partial_{x_i}\mathbf{u} = 0\end{gathered} \tag{2}$$

where

$$\dot{G} = \frac{\partial G(r,\tau)}{\partial\tau}, \qquad \tilde{\nabla} = (\partial_{x_i} r_j)\partial_{r_j} \tag{3}$$

The meshes are generated using the grid-generator Ogen, which has its basis in the CMPGRD algorithm by Chesshire and Henshaw [18]. A set of mappings are generated corresponding to the background mesh and the airfoil mesh, and each mapping maps the unit square to the physical domain. The solutions in the region of overlap are interpolated at appropriate interpolation points in the computational domain using a Lagrange interpolation formula in the form of $u_{ij} = \alpha\cdot u_{\mathrm{In}}$, where α and $\boldsymbol{u}_{\mathrm{In}}$ are second-order tensors that denote the interpolation weights and solutions from which the interpolation should be performed. Figure 1 shows a set of overlapping structured meshes in the vicinity of an airfoil. It can be seen from this figure that there are three sets of interpolation points, one for each mesh.

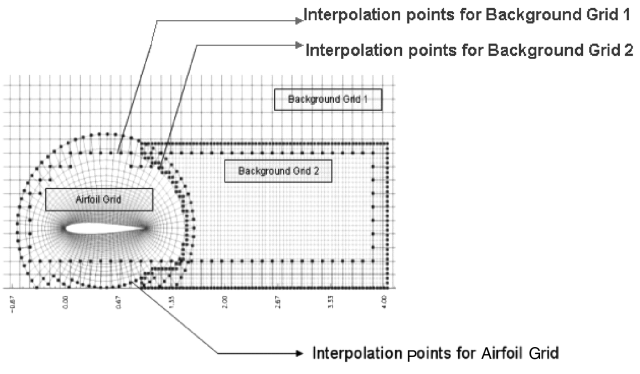

Fig. 1 A portion of the overlapping meshes used in the computation.

When the mesh moves, the location of the interpolation points also changes. In this process, some discretization points become interpolation points. Denoting $\mathbf{V}_i$ and p_i to be the discrete approximations to $\mathbf{U}$ and p respectively, the discretized equations take the following forms:

$$\frac{\mathrm{d}}{\mathrm{d}\tau}\mathbf{V}_i + [(\mathbf{V}_i - \dot{G}_i)\cdot\tilde{\nabla}_h] + \tilde{\nabla}_h\frac{p_i}{\rho} - \upsilon\tilde{\Delta}_h\mathbf{V}_i - F(x_i,t) = 0 \tag{4a}$$

$$\tilde{\Delta}_h p_i - \rho\Sigma_m\tilde{\nabla}_h V_{m,i}\cdot D_{m,h}\mathbf{V}_i - \rho C_{d,i}\tilde{\nabla}_h\cdot\mathbf{V}_i - \rho\tilde{\nabla}_h\cdot F(x_i,t) = 0 \tag{4b}$$

which are solved with the boundary conditions $B(\boldsymbol{V}_i, P_i) = 0$ and $\nabla_h\cdot\mathbf{V}_i = 0$ and initial conditions $\mathbf{V}(\boldsymbol{x}_i, 0) = \mathbf{U}_0(\boldsymbol{x}_i)$. The term $C_{d,i}$ appearing in Eq. (4b) is the divergence damping term [16]. The boundary condition for pressure is obtained by taking the dot product of the momentum equation with the normal. For moving boundaries, the boundary acceleration is also included and is given by

$$\frac{\partial p}{\partial n} = n\cdot(-\ddot{G} - \upsilon\tilde{\nabla}\times\tilde{\nabla}\times\mathrm{u}) \tag{5}$$

Equation (4b) is obtained as a result of taking divergence of the momentum equation, which results in a Poisson equation for pressure. The operators D and ∇_h are defined as follows:

$$D_{m,h} = \frac{\partial}{\partial x_m}, \qquad \nabla_h = (D_{1,h}, D_{2,h}, D_{3,h}) \tag{6}$$

where the subscript h is defined as a second- or fourth-order central-difference approximation. In this study, a second-order central discretization is used. The discretized equations are solved using a fractional step method that is second-order accurate for both pressure and velocity. Semi-implicit time stepping is used for advancing the solution in time. The discretization results in a set of linear equations that is solved by Oges [19], the overlapping mesh equation solver. Oges uses a variety of direct and iterative algorithms for sparse matrix computations. The GMRES [20] algorithm was used for all the computations shown in this paper. The pressure equation (4b) is also solved in a similar way.

A. Rigid-Body Dynamics

For test cases involving passive flight (i.e., rigid bodies moving under the action of aerodynamic forces and moments), the position and orientation of the rigid body needs to be determined at each time t. This information is obtained by solving the equations of motion for a rigid body and is implemented in the OverBlown code [16]. They are given by

$$M\frac{\mathrm{d}^2\mathbf{x}_{\mathrm{cm}}}{\mathrm{d}t^2} = \mathbf{F}_A \tag{7a}$$

$$\frac{\mathrm{d}\mathbf{h}}{\mathrm{d}t} = \mathbf{T} \tag{7b}$$

where $\mathbf{x}_{\mathrm{cm}}$ is the position of the center of mass, $\mathbf{h}$ is the angular momentum, $\mathbf{F}_A$ is the average aerodynamic force acting on the center of mass and is obtained as

$$\mathbf{F}_A = \int_{\mathrm{d}\Omega} pn_i - n_k\tau_{ki}\,\mathrm{d}S$$

and $\mathbf{T}$ is the torque defined by

$$\mathbf{T} = \int_{\mathrm{d}\Omega}(\mathbf{x}' - \mathbf{x}_{\mathrm{cm}})\,\mathrm{d}\mathbf{F}_A$$

where $\mathbf{x}'$ is any point on $\mathrm{d}\Omega$. Expressing the angular momentum $\mathbf{h}$ in terms of the principal moments of inertia I_i and angular velocity ω_i about the principle axes of inertia e_i as $\mathbf{h} = I_i\omega_i e_i$ will reduce Eq. (7b) to a system of ordinary differential equations, given by

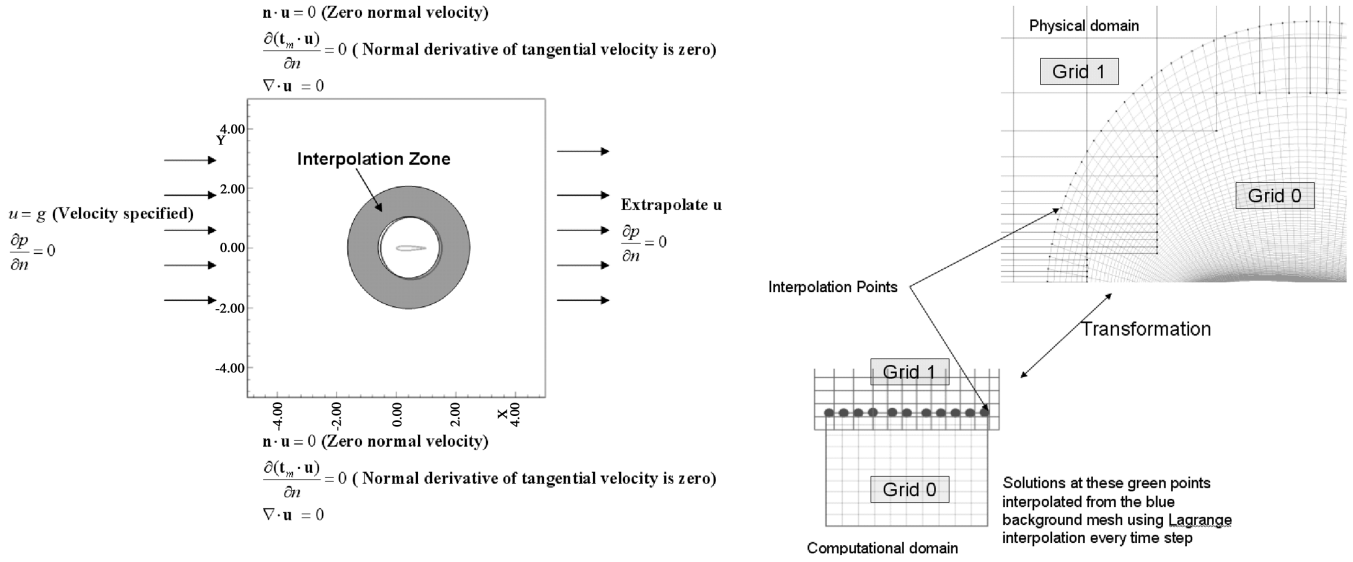

a) b)

Fig. 2 Problem setup for an overlapping mesh solution: a) physical domain with boundary conditions and b) interpolation zone.

$$I_i \dot{\omega}_i = \mathbf{T} \cdot e_i \tag{8a}$$

$$\dot{e}_i = \boldsymbol{\omega} \times e_i \tag{8b}$$

Equation (8b) is a consequence of the fact that the principle axes of inertia form an orthonormal basis. Equation (7a) along with Eqs. (8a) and (8b) are integrated in time to obtain the position of the center of mass and the principle axes. The acceleration due to the aerodynamic forces [obtained from Eq. (7a)] appears in the boundary condition for pressure in Eq. (5). The fluid dynamics equations are then solved with this boundary condition and a new set of forces are obtained. This process is repeated over a period of time till the final time of computation.

B. Physical Domain: Initial and Boundary Conditions

The momentum equation (4a) requires initial and boundary conditions on $\boldsymbol{u}$, and the pressure equation (4b) requires a boundary condition for p. For most of the unsteady problems involving plunging in a uniform flow, the flow is initialized with the corresponding steady-state flow solution. For a certain class of problems, a uniform flowfield is prescribed and they are projected to satisfy the divergence-free condition approximately at time $t = 0$. The difference between these types of initial conditions is highlighted in Sec. III.B. As for the boundary conditions for most of the problems involving moving bodies, Fig. 2a shows the physical domain along with the boundary conditions. At the inflow boundary, the far-field velocity is specified with a zero pressure gradient. At the outflow boundary, velocities are extrapolated from inside the domain, ensuring a zero pressure gradient. At the top and bottom boundaries, normal velocity and normal derivative of tangential velocity are set to zero to satisfy a divergence-free condition. Along the airfoil surface, the no-slip wall boundary condition is specified. The interpolation zone is handled as shown in Fig. 2b. The interpolation points for grid 0 are shown as dots in the physical and computational domain. The interpolation is performed in the computational domain. Using a Lagrange interpolation, the information (velocity and pressure) at these green dots (grid points) is obtained by interpolating the data from the blue mesh, which is grid 1. This type of interpolation results in accurate solutions if the solutions are smooth, although the discretization is nonconservative, as explained by Chesshire and Henshaw [18]. For nonsmooth solutions, Chesshire and Henshaw [21] have demonstrated a conservative interpolation scheme and applied it to a 2D viscous Burgers equation with a shock. Boundary conditions for pressure on the body surface are obtained from Eq. (5). This boundary condition has an intrinsic divergence-free condition.

III. Validation Studies for the OverBlown Code

To assess the accuracy of the OverBlown code, several validation studies were conducted for unsteady and steady flows on static and moving meshes based on available computational/experimental results.

A. Mesh Dependency Study for a Plunging Airfoil

The effect of mesh size on the numerical accuracy is an important aspect in assessing the quality of a flow solution. Here, a plunging (oscillations along a vertical plane) airfoil is considered with different mesh sizes and the aerodynamic force coefficients are compared. A sinusoidal displacement $h = h_0 \sin(2\pi f t)$ with amplitude $h_0 = 0.12$ and frequency $f = 0.979$ Hz is prescribed for the airfoil. The flow Reynolds number is 500 and the Strouhal number is 1.5. Four mesh systems are considered, each mesh system consisting of three overlapping meshes, a background Cartesian mesh, an airfoil curvilinear mesh, and a wake Cartesian mesh. The details of the mesh are summarized in Table 1. When the airfoil moves, the airfoil mesh and the wake mesh move rigidly with the airfoil.

The flow is initialized with a steady flowfield and the solutions are computed at regular intervals of time. Figure 3 shows the computed time histories of aerodynamic lift and drag coefficients on the four mesh systems, along with a close-up view of the peak lift and drag coefficients. It can be seen that on the coarse mesh, the minimum drag

Table 1 Various meshes considered for convergence studies

Component mesh	Mesh system 1	Mesh system 2	Mesh system 3	Mesh system 4
Square (background)	30 × 30	30 × 30	41 × 41	81 × 81
Wake	20 × 20	30 × 30	61 × 61	121 × 121
Airfoil	30 × 30	60 × 35	121 × 71	242 × 142

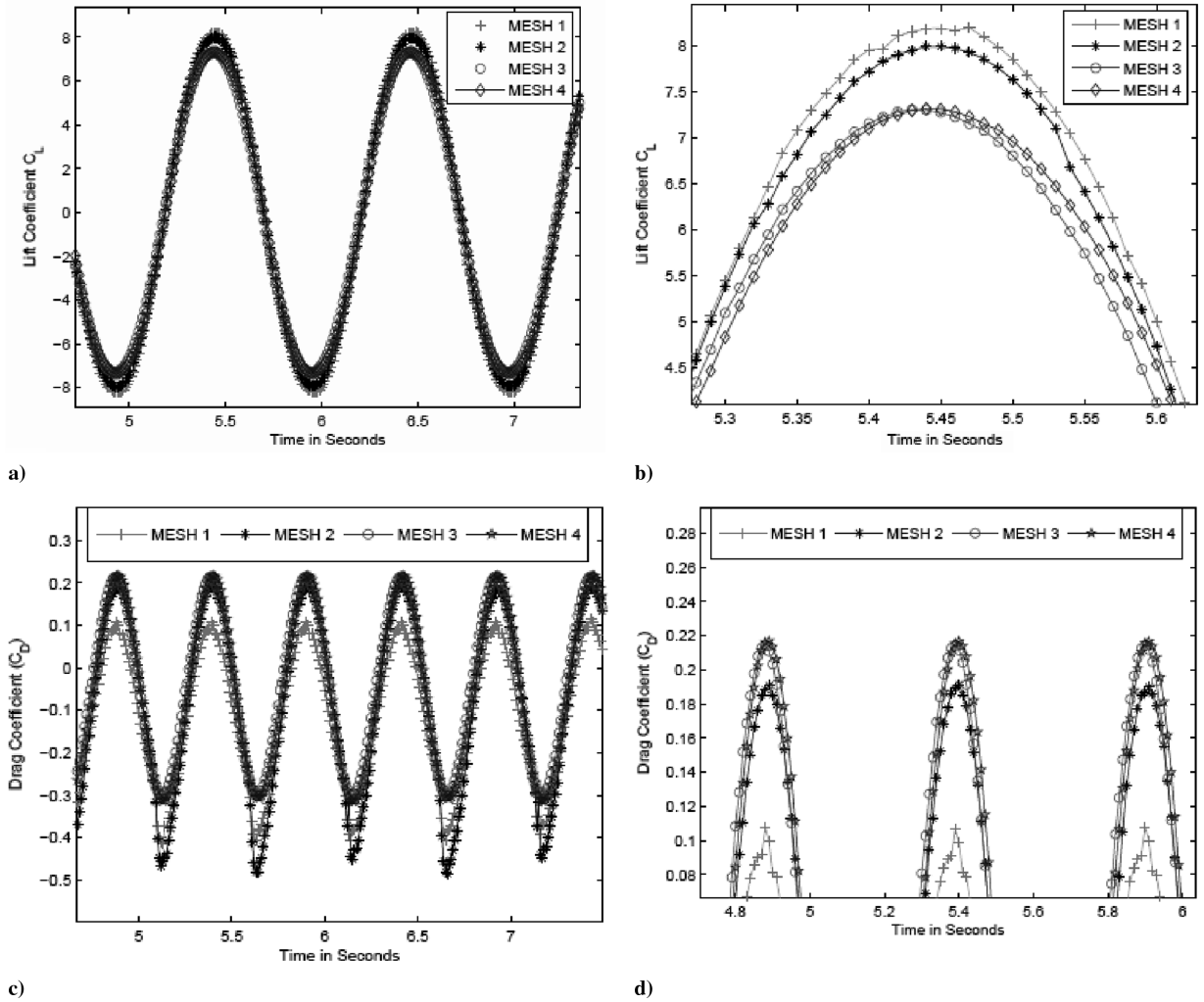

Fig. 3 Aerodynamic coefficients for different meshes: a) lift coefficient, b) near view of the lift coefficient, c) drag coefficient, and d) near view of the drag coefficient.

coefficient is underpredicted (or the thrust is maximum). This has a direct implication on the forward flight arising due to plunging motion. An airfoil set in motion will travel faster when the solutions are computed on a coarse mesh due to higher thrust coefficients. Defining average lift and drag coefficients is not proper for unsteady flows in general, whether they are periodic or not. For example, when the forward flight of an insect or a bird is considered, it is the instantaneous lift/thrust coefficient that dictates the entire motion and not the average force coefficients. However, for the purposes of obtaining quantitative results for a mesh dependency study, the force coefficients are averaged out over one cycle. For the present computation, the average value of lift and drag coefficients are obtained in the interval of $6 < t < 7$ s. These average quantities are plotted as a function of $\log(1/N)$, where N is the total number of mesh points used for a given mesh system and is shown in Fig. 4.

The lift and drag coefficients reach a value of 0.069 and −0.0497, respectively, in an asymptotical manner. The negative drag coefficient indicates that the airfoil is producing thrust. Using the airfoil mesh as a reference and a mesh refinement ratio of $r_m = 2$, the observed order of convergence as outlined in Roache [22] is estimated using three values of the lift coefficient: $C_{L_1} = 0.069$, $C_{L_2} = 0.0773$, and $C_{L_3} = 0.119$, where C_{L_1}, C_{L_2}, and C_{L_3} are the lift coefficients obtained on mesh systems 4, 3, and 2, respectively. The observed order of convergence turns out to be

$$p = \frac{1}{\ell n(r_m)} \ell n\left(\frac{C_{L_3} - C_{L_2}}{C_{L_2} - C_{L_1}}\right) = 2.06$$

An estimate of the grid convergence index as outlined in Roache [22] for the fine mesh (mesh system 4); that is,

$$\mathrm{GC}I = \frac{Fs|\varepsilon|}{r_m^p - 1}$$

where $F_s = 1.25$ is a factor of safety when comparing three or more meshes, and

$$\varepsilon = \frac{C_{L_2} - C_{L_1}}{C_{L_1}}$$

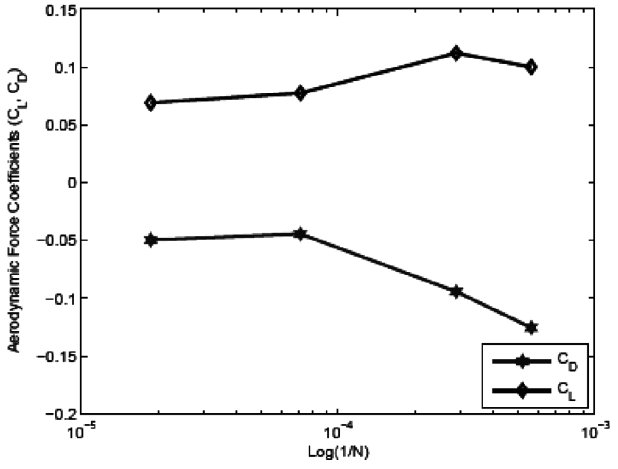

Fig. 4 Time-averaged lift and drag coefficients as a function of mesh points.

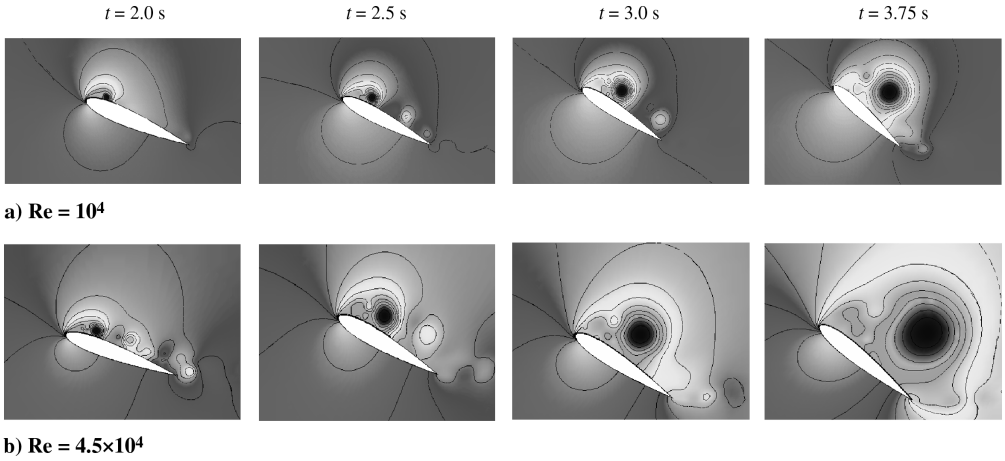

Fig. 5 Pressure contours for a rapidly pitching airfoil at a) $Re = 10^4$ on a 200 × 100 mesh and b) $Re = 4.5 \times 10^4$ on a 300 × 50 mesh.

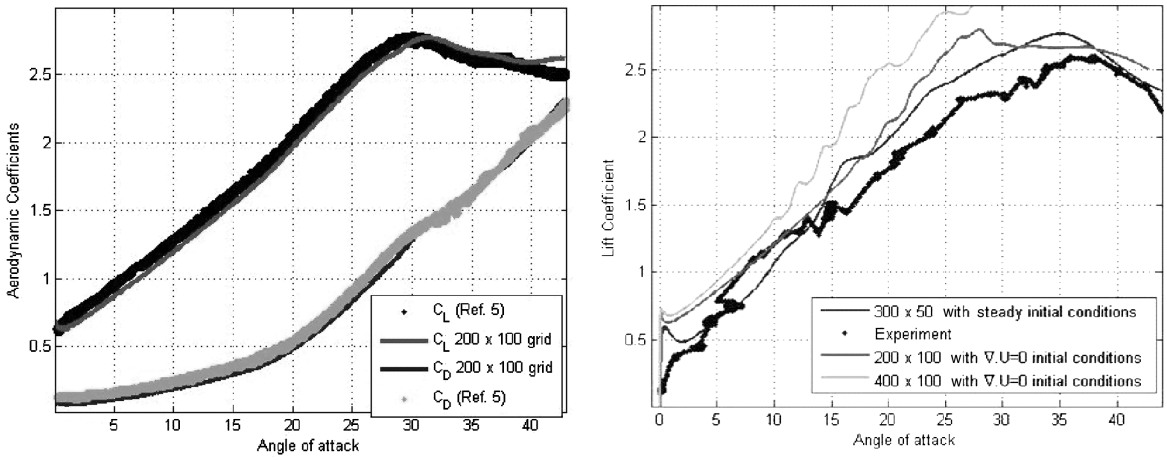

a) b)

Fig. 6 Computed aerodynamic characteristics for a rapidly pitching airfoil at a) $Re = 10^4$ and b) $Re = 4.5 \times 10^4$ on various meshes.

turns out to be 0.0483. The small value of the grid convergence index indicates that the solution is in the asymptotic range of convergence. Mesh system 4 is thus used in most of the computations for Reynolds numbers on the order of 100–1000.

B. Rapid Pitching of a NACA 0015 Airfoil: Simulation of Airfoil Dynamic Stall

Dynamic stall in airfoils has been the subject for many researchers for the past few decades. A wide range of experiments reported in McCroskey et al. [23] and numerical computations by Liu and Kawachi [5], Visbal and Gordnier [24], Van Dyken et al. [25], and Visbal and Shang [26] have been performed to study the unsteady separation and the formation of dynamic stall vortex and its impact on lift augmentation in pitching airfoils. Following the lines of Visbal and Shang [26] and Lui and Kawachi [5], the rapid pitching of a NACA 0015 airfoil about the quarter-chord position from a 0-deg angle of attack to a maximum of 45 deg is demonstrated. The temporal variation of angular velocity is given by $\Omega(t) = \Omega_0(1 - e^{-4.6t/t_0})$ $(t \geq 0)$, where $t_0 = 0.5$ is the time taken to reach 99% of the final angular velocity $\Omega_0 = 0.2$. For $Re = 10^4$, computations were carried out on a 200×100 mesh around the airfoil and 80×80 background mesh with initial conditions projected so that the divergence condition $\nabla \cdot U = 0$ is satisfied at $t = 0$. For $Re = 4.5 \times 10^4$, computations were carried out on 200×100 and 400×100 airfoil meshes with $\nabla \cdot U = 0$ as the initial condition and a 300×50 airfoil mesh with steady flow initial conditions. For $Re = 10^4$, the present computational results are compared with that of Liu and Kawachi [5], and for $Re = 4.5 \times 10^4$, computational results are compared with the experimental results cited in Visbal and Shang [26]. Figures 5a and 5b show the computed pressure contours for the two cases of Reynolds numbers at various times $t = 2.0$, 2.5, 3.0, and 3.75 s, respectively. The flow features are very similar for both these Reynolds numbers, except for the fact that finer structures are observed for the higher-Reynolds-numbers case. The leading-edge vortex is seen to develop and convect downstream of the airfoil.

Figure 6a shows the comparison of the computed variations of C_L and C_D with angle of attack for $Re = 10^4$ with the computational results of Liu [5]. It can be seen that the results of the present computation are in good agreement, thereby justifying the laminar assumption at these Reynolds numbers. Figure 6b shows the corresponding lift and drag characteristics for $Re = 4.5 \times 10^4$. The lift coefficient maintains a very high value till about 30 deg for $Re = 10^4$ and 35 deg for $Re = 4.5 \times 10^4$. It can also be seen from Fig. 5 that the vortex detachment is accompanied by a loss in lift (Fig. 6). The position of $C_{L_{\max}}$ is in good agreement with the experimental results when the steady flow initial conditions were used. This is expected, because the experiment was also conducted in a similar manner. The results from an arbitrary divergence-free condition do not converge to the experimental conditions; it can be seen from Fig. 6b that by mesh refinement, the computations converge to a wrong solution.

IV. Influence of Airfoil Trailing-Edge Profiles on Active and Passive Plunging Aerodynamics

The effect of trailing-edge topology on the performance of plunging airfoils is investigated. A base airfoil such as NACA 0012 with a finite trailing-edge angle is considered. Assuming that y =

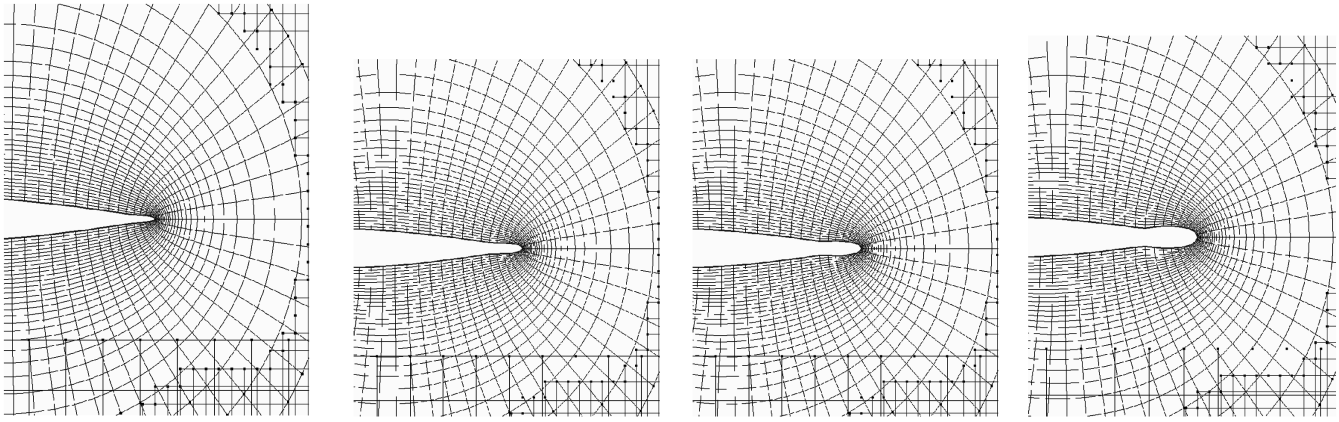

Case 1: r=0.08 Case 2: r=0.12 Case 3: r=0.15 Case 4: r=0.18

Fig. 7 Airfoil trailing-edge topology for different roundness parameters.

$y(x)$ describes the shape of the base airfoil and r ($r \neq 0$) denotes the trailing-edge roundness parameter [17], then the portion of the airfoil in the range of $1 - r \leq x \leq 1$ is altered according to

$$Y(x) = y(x) + \frac{x - (1 - r)}{r}[r\sqrt{1 - x} - y(x)]$$

where $Y(x)$ denotes the shape of the new airfoil with the modified trailing-edge topologies. Active flight computations were carried out for the original base airfoil and on modified airfoils using $r = 0.08$, 0.12, 0.15, and 0.18 (shown in Fig. 7) and also with ground effect ($z/c = 1.5$) and without ground effect. Passive flight computations were carried out for the same trailing-edge topologies as that of active flight with ground effect. Apart from ground vicinity and trailing-edge topology, the plunging performance in zero freestream velocity and finite freestream velocity for active flight is compared. For passive flight, there is no freestream flow imposed and the airfoil plunges to find its path.

A. Active Flight

Computed wake structures of a plunging NACA 0012 airfoil are first compared for $k = 10.1$ and $h_0 = 0.2$ with the experimental results of Jones et al. [27]. The Reynolds number for this case was 500. Computations were performed using a unit freestream velocity specified at the inlet, from which the fluid viscosity is obtained based on the Reynolds number. The displacement follows the equation $h = h_0[1 - \cos(2\pi ft)]$. The mesh system is shown in Fig. 7. It consists of three meshes, a moving airfoil mesh that moves rigidly with the airfoil, a Cartesian wake mesh, and a background Cartesian mesh. For all the cases considered, mesh system 4 was adopted and the first mesh point is located at a distance of $3.6 \times 10^{-5}c$ from the airfoil surface. Under these conditions, a deflected vortex street (dual mode) was observed experimentally, and the direction of the jet can be seen to be dependent on initial conditions. Figure 8a shows the computed vortex structures at $t = 2.2$ s and is compared with the corresponding experimental measurements in Fig. 8b. The agreement between the computational and experimentally visualized flow structures can be seen to be quite good in terms of the initial jet deflection.

Heathcote and Gursul [28] also observed the jet to be switching directions periodically at high Reynolds numbers ($\sim$20, 000) when plunged in zero freestream conditions, as shown in Fig. 8c. For the current study, computed vortex structures in zero freestream and finite freestream conditions shown in Figs. 8d and 8e also show this phenomenon. This also results in the lift coefficient to be periodic about a positive value for some period of time and then negative for rest of the time after 50 plunge cycles, as shown in Fig. 9.

Figure 10 shows the computed airfoil wake structures from the present study. Figure 10a shows that altering the trailing-edge radius to case 4 ($r = 0.18$) results in the reduction of the wake-deflection angle by a small amount. Figure 10b shows a portion of the interpolation zone when the vortex is in the overlapping region. It can be seen that the contours are continuous across the overlap region, confirming a proper implementation of the algorithm on the system of overlapping meshes. The effect of trailing-edge radius on the aerodynamic forces will be discussed subsequently. Instantaneous streamlines in the reference frame of the moving airfoil for the original base airfoil as well as for the modified airfoil (case 4) are shown in Fig. 11 after the instant when the airfoil has just reached its maximum position at $t = 3.5$ s. For the base airfoil, it can be seen that

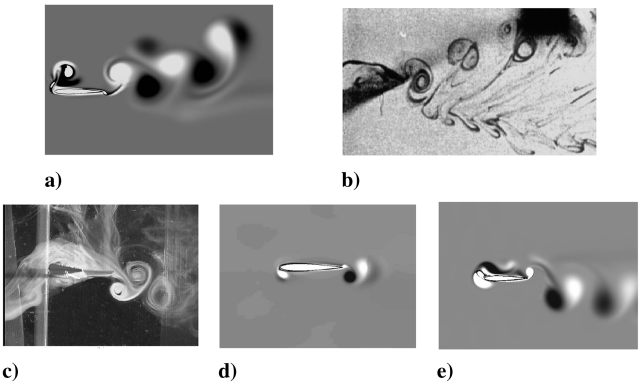

a) b) c) d) e)

Fig. 8 Plunging airfoil wake structures for $k = 10.1$ and $h_0 = 0.2$: a) current computation b) experiments from [27], c) experiments from [28] at a later instant of time, d) computation with zero freestream conditions, and e) computation with finite freestream conditions.

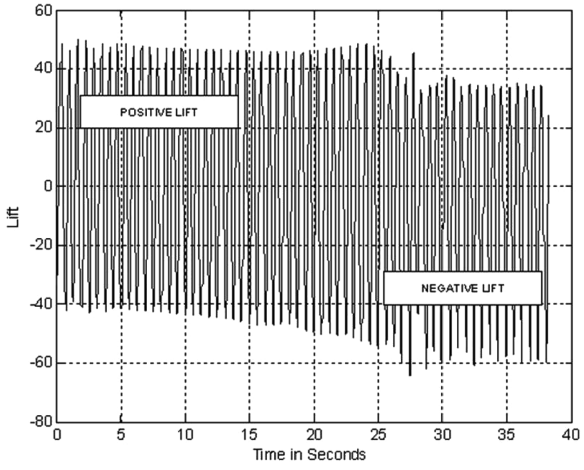

Fig. 9 Lift of a plunging airfoil with a dual-mode vortex street ($k = 10.0$ and $h_0 = 0.2$).

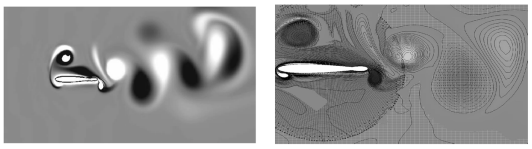

a) b)

Fig. 10 Wake structures behind a plunging airfoil for case 4: a) vorticity contours and b) the overlap region showing the interpolation points around airfoil mesh and vorticity contours.

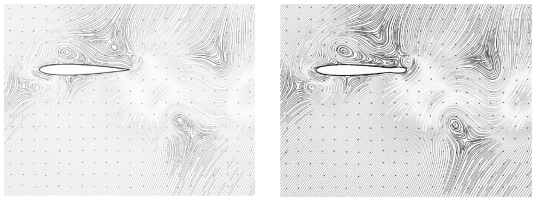

a) b)

Fig. 11 Instantaneous streamlines for a plunging airfoil: a) base airfoil and b) airfoil case 4 at $t = 3.5$ s.

the vortex at the trailing edge has already separated and some amount of fluid has made its way to the upper side on the trailing edge. However, for the modified airfoil, the trailing-edge vortex is still attached to the airfoil, giving rise to a larger effective body thickness. This results in increased drag, hence lowering the thrust.

Additional computations were carried out for an airfoil that was plunged at a frequency $k = 12.3$, corresponding to the case in which the nondimensional amplitude $h_0 = 0.06$, such that the Strouhal number $St = 0.738$ and the Reynolds number $Re = 500$. Instantaneous aerodynamic lift, thrust, and moment coefficients were estimated for all conditions specified previously. The Strouhal number based on the peak plunge velocity is defined only for flows with a finite freestream velocity. Hence, for these types of flows, lift and thrust coefficients can be estimated as $2\boldsymbol{F}_A/\rho u_\infty^2$, where $\boldsymbol{F}_A$ is the instantaneous vector of aerodynamic forces and is given by

$$\boldsymbol{F}_A = \int_{\mathrm{d}\Omega} pn_i - n_k \tau_{ki}\,\mathrm{d}S$$

For the plunging motion of the airfoil at zero freestream velocity, the only velocity scale available is the peak plunge velocity, $V_p = 2\pi f h_0 c$. Hence, it is appropriate to use this velocity scale for plunging in zero freestream conditions. However, for the sake of comparing cases involving finite and zero freestream conditions, the peak plunge velocity is used to nondimensionalize the forces for all cases. Figure 12 shows the instantaneous drag coefficients without

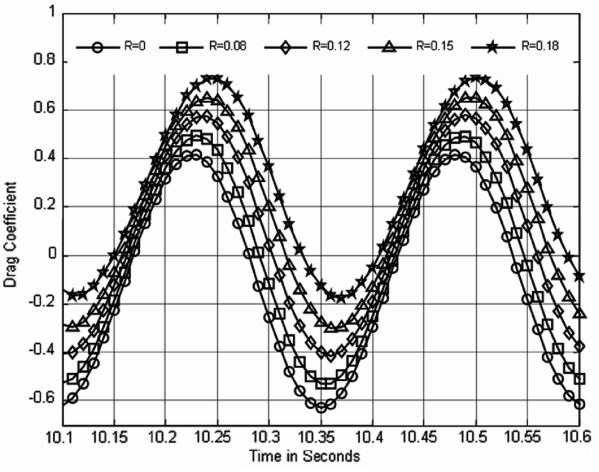

a)

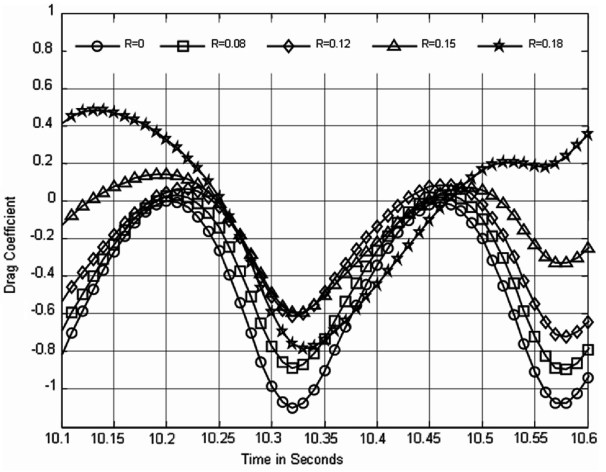

b)

Fig. 12 Time history of the drag coefficient for plunging airfoils: a) finite freestream and b) zero freestream.

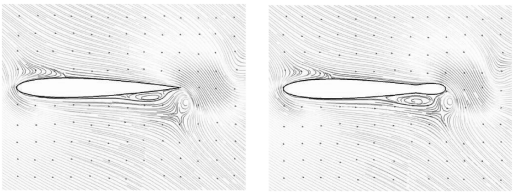

a) b)

Fig. 13 Instantaneous streamlines for a plunging a) base airfoil and b) case 4 airfoil at its mean position.

ground effect for plunging in finite and zero freestream conditions. It is clearly observed that as the trailing-edge radius is reduced, the drag curve shifts vertically downward, indicative of more thrust. The corresponding streamlines for the base airfoil and the airfoil with case 4 are shown in Fig. 13 when the airfoil is in the mean position moving upward. These figures are consistent with the observation in Fig. 11 that effective body thickness increases the drag. The lift coefficient is not shown, due to the fact that it remains almost symmetric during the upper and lower halves of the plunging cycle, giving rise to a zero time-averaged lift coefficient, unlike for the case involving a dual-mode vortex street in Fig. 9.

Plunging in ground effect either increases or decreases the thrust at selected points in the plunging cycle. Figure 14 shows the plunge displacement and velocity with time, and Fig. 15 shows a comparison of the drag coefficient with and without ground effect in the presence of a finite freestream flow. It is observed that drag increases with ground effect at the end points of the cycle (i.e., when the airfoil crosses $h = 0$ and $h = 2h_0$), precisely during the upstroke. But during the downstroke, as the airfoil passes through its mean position (when velocity is maximum), the presence of the ground increases thrust.

Time-averaged velocity profiles downstream of the airfoil at a distance $0.4c$ are plotted in Fig. 16 for the base airfoil and for the airfoil for case 4. These results show that the sharper trailing-edge airfoil produces a jet with higher velocity and hence higher thrust.

B. Passive Flight: Effect of the Trailing Edge

The need for a sharp airfoil trailing edge for efficient thrust generation is demonstrated based on coupled Navier–Stokes rigid-body computations on plunging foils near the ground. Gravity is not employed in all of these test cases, because the effect of plunging on thrust/lift production is studied. The Reynolds number for these cases varied from 2000–4500, based on the forward speed. The airfoil is plunged at a frequency of $f = 0.979$ Hz with an amplitude of $h_0 = 0.12$ and follows a sinusoidal displacement $h = h_0 \sin(2\pi f t)$. The mesh system consists of a mesh surrounding the airfoil overlapping a background Cartesian mesh, as shown in Fig. 7.

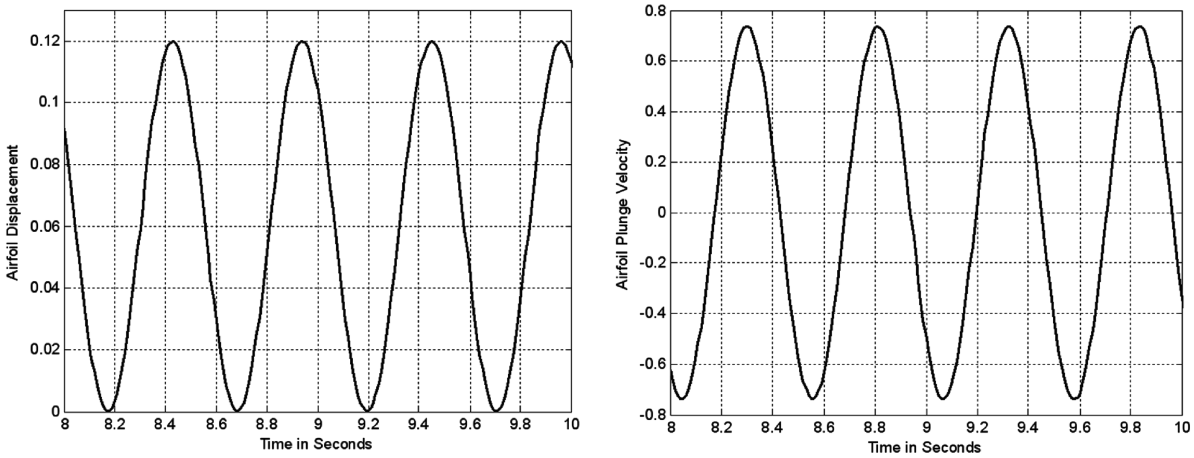

a) b)

Fig. 14 Airfoil plunging kinematics: a) plunge displacement and b) plunge velocity.

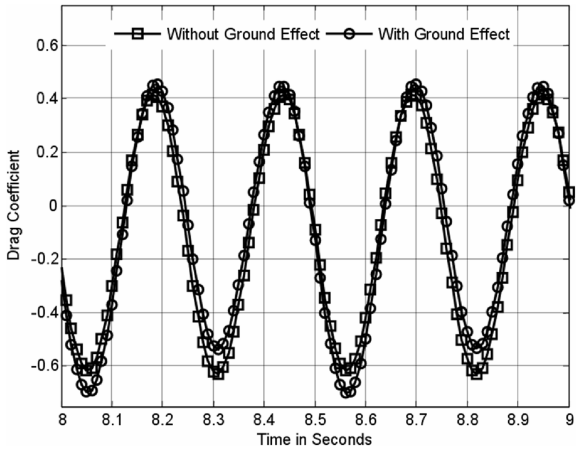

Fig. 15 Comparison of the time history of the drag coefficient with and without ground effect.

The mesh surrounding the airfoil moves rigidly with the airfoil and the background Cartesian mesh is fixed. The rigid-body motion is simultaneously determined at each time step from the forces. At this amplitude and frequency, it is known from the previous section that this configuration will generate thrust. This is evident from Figs. 17 and 18, in which we observe the airfoil motion toward the left as a result of thrust generation. Figure 17 shows the computed

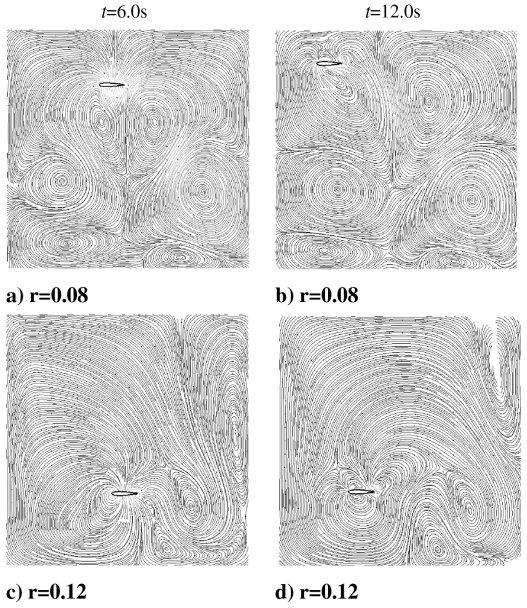

a) r=0.08 b) r=0.08

c) r=0.12 d) r=0.12

Fig. 17 Streamlines with regard to the inertial frame for passive flight at various times and cases.

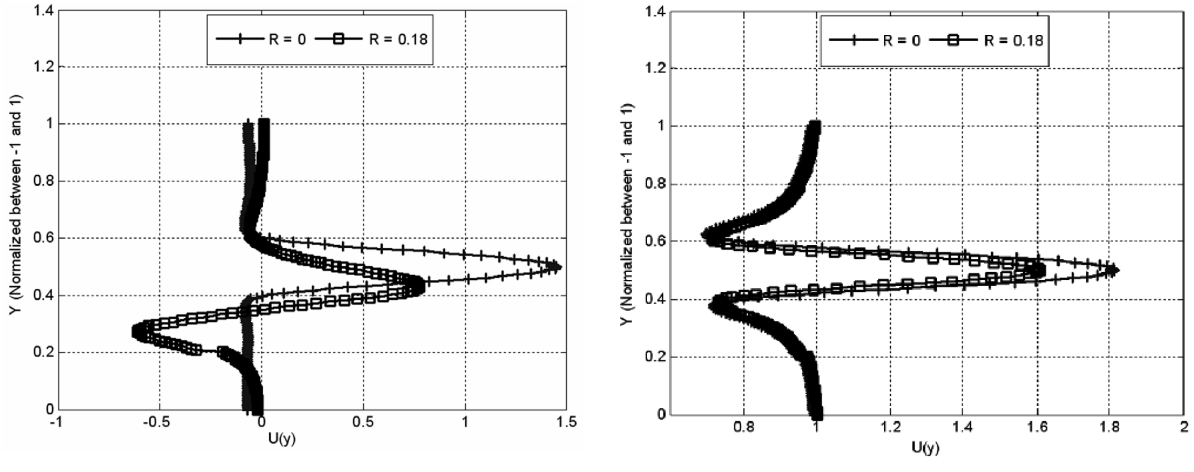

a) b)

Fig. 16 Time-averaged velocity profiles downstream of the airfoil at located at 0.4 *c* aft the trailing edge for plunging in a) zero freestream and b) finite freestream conditions.

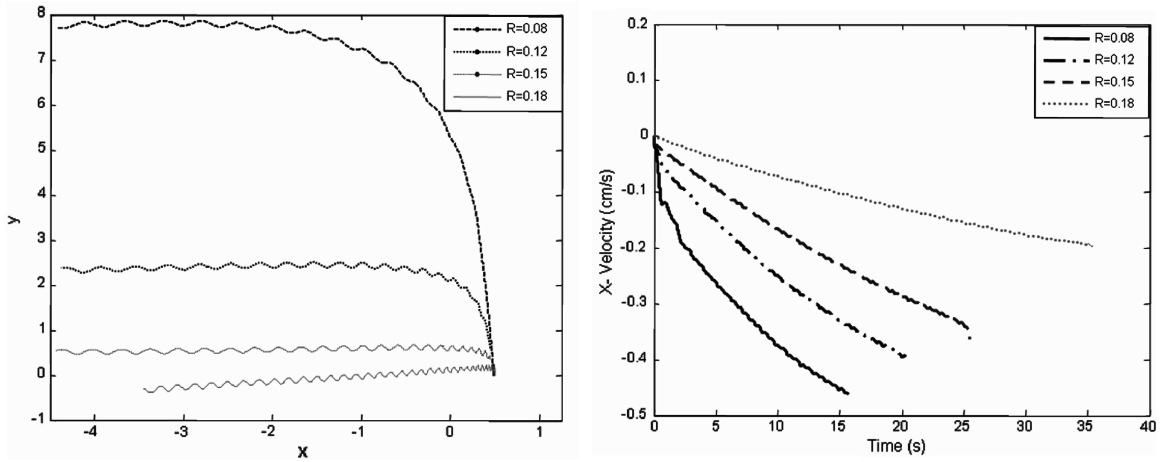

a) b)

Fig. 18 Trajectory of the airfoil for different a) trailing-edge roundness parameters and b) forward speed.

streamlines in the inertial frame of reference for $r = 0.08$ and 0.12 at times $t = 6$ and 12 s, respectively.

Figure 18 shows the path of the airfoil and forward speed attained for different trailing-edge roundness parameters. The periodic behavior in the trajectory is obtained approximately after 10 cycles. It is seen that with decreasing roundness, more thrust is generated and the airfoil travels faster. It is also observed that the airfoil plunges to a higher altitude for a stable position with increasing trailing-edge sharpness. This can readily be explained when the lift coefficient history is examined for an airfoil-plunged-in-ground effect. The initial $C_{L\max}$ for sharper trailing edges is relatively higher during the first cycle when compared with blunt trailing edges. This could possibly be due to the presence of the ground. It is unknown, however, whether these initial transients are physical or numerical.

IV. Conclusions

Computation of an unsteady low-Reynolds-number flowfield past moving airfoils was carried out by solving the unsteady incompressible Navier–Stokes equations on a system of overlapping and moving meshes using structured grids. Unsteady flows are created by moving overlapping meshes relative to one another. The effects of initial conditions for a rapidly pitching airfoil in incompressible low-Reynolds-number flow were discussed and solutions were computed on different meshes. It was also shown that for two-dimensional computations, the sharpness of the airfoil trailing edge has a marked effect on the thrust generated when the airfoil is plunged sinusoidally in zero freestream and finite freestream conditions. The rigid-body dynamics of plunging airfoils show a phenomenal result that airfoils with sharp trailing edges travel faster than rounded trailing edges. From these results, it can also be inferred that the asymmetry of the leading and trailing edges plays an important role in thrust production. Active and passive pitching and plunging motions of airfoils were considered in this study. Passive unsteady motion results in the computation of the airfoil trajectories during the simulation via a coupling between the fluid dynamics and the dynamics of motion. This study sets the basis for the computational study of three-dimensional low-Reynolds-number flapping-wing aerodynamics, which will be reported in a separate paper.

Acknowledgments

The authors would like to thank William D. Henshaw, Center for Applied Scientific Computing (CASC), Lawrence Livermore National Laboratory, University of California, for his valuable suggestions and comments and for the extensive usage of the OverBlown/Overture code.

References

[1] Sun, M., and Tang, J., "Unsteady Aerodynamic Force Generation by a Model Fruit Fly Wing in Flapping Motion," *The Journal of Experimental Biology*, Vol. 205, No. 1, Jan. 2002, pp. 55–70; also http://jeb.biologists.org/cgi/content/abstract/205/1/55 [retrieved 17 November 2007].

[2] Ramamurti, R., Sandberg, W. C., Lohner, R., Walker, J. A., and Westneat, M. W., "Fluid Dynamics of Flapping Aquatic Flight in the Bird Wrasse: Three-Dimensional Unsteady Computations with Fin Deformation," *The Journal of Experimental Biology*, Vol. 205, No. 19, Oct. 2002, pp. 2997–3008; also http://jeb.biologists.org/cgi/content/abstract/205/19/2997 [retrieved 17 November 2007].

[3] Ellington, C. P., "The Novel Aerodynamics of Insect Flight: Applications to Micro-Air Vehicles," *The Journal of Experimental Biology*, Vol. 202, No. 23, Dec. 1999, pp. 3439–3448; also http://jeb.biologists.org/cgi/content/abstract/202/23/3439 [retrieved 17 November 2007].

[4] Shyy, W., Berg, M., and Ljungqvist, D., "Flapping and Flexible Wings for Biological and Micro-Air Vehicles," *Progress in Aerospace Sciences*, Vol. 35, No. 5, July 1999, pp. 455–505. doi:10.1016/S0376-0421(98)00016-5

[5] Liu, H., and Kawachi, K., "A Numerical Study of Insect Flight," *Journal of Computational Physics*, Vol. 146, No. 1, Oct. 1998, pp. 124–156. doi:10.1006/jcph.1998.6019

[6] Wang, Z. J., Birch, J. M., and Dickinson, M. H., "Unsteady Forces and Flows in Low Reynolds Number Hovering Flight: Two-Dimensional Computations vs Robotic Wing Experiments," *The Journal of Experimental Biology*, Vol. 207, No. 3,Jan. 2004, pp. 449–460; also http://jeb.biologists.org/cgi/content/full/207/3/449 [retrieved 17 November 2007]. doi:10.1242/jeb.00739

[7] Liu, H., Ellington, C. P., Kawachi, K., Van Den Berg, C., and Willmott, A. P., "A Computational Fluid Dynamic Study of Hawkmoth Hovering," *The Journal of Experimental Biology*, Vol. 201, No. 4, Feb. 1998, pp. 461–477; also http://jeb.biologists.org/cgi/content/short/201/4/461 [retrieved 17 November 2007].

[8] Tuncer, I. H., and Platzer, M. F., "Computational Study of Flapping Airfoil Aerodynamics," *Journal of Aircraft*, Vol. 37, No. 3, 2000, pp. 514–520.

[9] Jones, K. D., Dohring, C. M., and Platzer, M. F., "Experimental and Computational Investigation of the Knoller-Betz Effect," *AIAA Journal*, Vol. 36, No. 7, 1998, pp. 1240–1246.

[10] Sengupta, T. K., Vikas, V., and Johri, A., "An Improved Method for Calculating Flow Past Flapping and Hovering Airfoils," *Theoretical and Computational Fluid Dynamics*, Vol. 19, No. 6, 2005, pp. 417–440. doi:10.1007/s00162-005-0003-9

[11] Tuncer, I. H., and Platzer, M. F., "Thrust Generation Due to Airfoil Flapping," *AIAA Journal*, Vol. 34, No. 2, 1996, pp. 324–331.

[12] Pesavento, U., and Wang, Z. J., "Falling Paper: Navier–Stokes Solutions, Model of Fluid Forces, and Center of Mass Elevation," *Physical Review Letters*, Vol. 93, No. 14, Oct. 2004, pp. 144501-1–144501-4.

doi:10.1103/PhysRevLett.93.144501
[13] Lai, C. S. J., and Platzer, M. F., "Characteristics of a Plunging Airfoil at Zero Freestream Velocity," *AIAA Journal*, Vol. 39, No. 3, 2001, pp. 531–534.
[14] Bennet, A. G., Obye, R. C., and Jeglum, P. M., "Ornithopter Aerodynamic Experiments," *Swimming and Flying in Nature*, Vol. 2, Plenum Press, New York, 1975, pp. 985–1000.
[15] Jones, K. D., Castro, B. M., Mahmoud, O., and Platzer, M. F., "A Numerical and Experimental Investigation of Flapping Wing Propulsion in Ground Effect," 40th Aerospace Sciences Meeting & Exhibit, AIAA Paper 2002-866, 2002.
[16] Henshaw, W. D., "OverBlown: A Fluid Flow Solver for Overlapping Grids, Reference Guide, Version 1.0," Univ. of California Radiation Lab., Paper MA-134289, 2003, pp. 1–51.
[17] Brown, D. L., Chesshire, G. S., Henshaw, W. D., and Quinlan, D. J., "Overture: An Object Oriented Software System for Solving Partial Differential Equations in Serial and Parallel Environments," Eighth Conference on Parallel Processing for Scientific Computing, Society for Industrial and Applied Mathematics Paper CP97, 1997.
[18] Chesshire, G., and Henshaw, W. D., "Composite Overlapping Meshes for the Solution of Partial Differential Equations," *Journal of Computational Physics*, Vol. 90, No. 1, 1990, pp. 1–64. doi:10.1016/0021-9991(90)90196-8
[19] Henshaw, W. D., and Fast, P., "Oges: A Solver for Steady State Boundary Value Problems, User Guide, Version 2.0," Univ. of California Radiation Lab., Paper MA-132234, 2003, pp. 1–23.
[20] Saad, Y., and Schultz, M., "GMRES: A Generalized Minimal Residual Algorithm for Solving Nonsymmetric Linear Systems," *SIAM Journal on Scientific and Statistical Computing*, Vol. 7, No. 3, July 1986, pp. 856–869. doi:10.1137/0907058
[21] Chesshire, G., and Henshaw, W. D., "A Scheme for Conservative Interpolation on Overlapping Grids," *SIAM Journal on Scientific Computing*, Vol. 15, No. 4, 1994, pp. 819–845. doi:10.1137/0915051
[22] Roache, P. J., *Verification and Validation in Computational Science and Engineering*, Hermosa, Albuquerque, NM, 1998.
[23] McCroskey, W. J., Carr, L. W., and McAlister, K. W., "Dynamic Stall Experiments on Oscillating Airfoils," 13th AIAA Aerospace Sciences Meeting, Pasadena, CA, AIAA Paper 1975-125, 20–22 Jan. 1975.
[24] Visbal, M. R., and Gordnier, R. E., "A High Order Flow Solver for Deforming and Moving Meshes," *Fluids 2000*, AIAA Paper 2000-2619, 2000.
[25] Van Dyken, R. D., Ekaterinaris, J. A., Chandrasekhara, M. S., and Platzer, M. F., "Analysis of Compressible Light Dynamic Stall Flow at Transitional Reynolds Numbers," *AIAA Journal*, Vol. 34, No. 7, 1996, pp. 1420–1427.
[26] Visbal, M. R., and Shang, J. S., "Investigation of the Flow Structure Around a Rapidly Pitching Airfoil," *AIAA Journal*, Vol. 27, No. 8, 1989, pp. 1044–1051.
[27] Jones, J. D., Dohring, C. M., and Platzer, M. F., "Wake Structures Behind Plunging Airfoils: A Comparison of Numerical and Experimental Results," 34th Aerospace Sciences Meeting and Exhibit, Reno, NV, AIAA Paper 96-0078, 1996.
[28] Heathcote, S., and Gursul, I., "Jet Switching Phenomena for a Plunging Airfoil," 34th Fluid Dynamics Conference and Exhibit, Portland, OR, AIAA Paper 2004-2150, 2004.

Z. Wang
Associate Editor